

# Superfluorescence from Lead Halide Perovskite Quantum Dot Superlattices

Gabriele Rainò<sup>1,2,3\*</sup>, Michael A. Becker<sup>3,4\*</sup>, Maryna I. Bodnarchuk<sup>2</sup>, Rainer F. Mahrt<sup>3</sup>, Maksym V. Kovalenko<sup>1,2</sup>, and Thilo Stöferle<sup>3</sup>

<sup>1</sup>Institute of Inorganic Chemistry, Department of Chemistry and Applied Bioscience, ETH Zurich, 8093 Zurich, Switzerland.

<sup>2</sup>Laboratory of Thin Films and Photovoltaics, Empa – Swiss Federal Laboratories for Materials Science and Technology, 8600 Dübendorf, Switzerland.

<sup>3</sup>IBM Research – Zurich, Säumerstrasse 4, 8803 Rüschlikon, Switzerland.

<sup>4</sup>Optical Materials Engineering Laboratory, ETH Zurich, 8092 Zurich, Switzerland.

\* These authors contributed equally to this work.

**An ensemble of emitters can behave significantly different from its individual constituents when interacting coherently via a common light field. After excitation, collective coupling gives rise to an intriguing many-body quantum phenomenon, resulting in short, intense bursts of light: so-called superfluorescence<sup>1</sup>. Because it requires a fine balance of interactions between the emitters and their decoupling from the environment, together with close identity of the individual emitters, superfluorescence has thus far been observed only in a limited number of very specific systems, such as certain atomic and molecular gases and a few select solid-state systems<sup>2-7</sup>. With colloidal nanocrystals, however, which are increasingly recognized as bright, practically suited photonic sources for optoelectronics<sup>8,9</sup>, the generation of superfluorescent light was precluded by inhomogeneous emission broadening, low oscillator strength, and fast exciton dephasing. Using caesium lead halide (CsPbX<sub>3</sub>, X = Cl, Br) perovskite nanocrystals<sup>10-13</sup> that are self-organized into highly ordered three-dimensional superlattices allows us to observe key signatures of superfluorescence: dynamically red-shifted emission with more than twenty-fold accelerated radiative decay, extension of the first-order coherence time by more than a factor of four,**

**photon bunching, and delayed emission pulses with Burnham–Chiao ringing behaviour<sup>14</sup> at high excitation density. These mesoscopically extended coherent states can be employed to boost opto-electronic device performances<sup>15</sup> and enable entangled multi-photon quantum light sources<sup>16,17</sup>.**

Spontaneous emission (SE) of photons, such as fluorescence commonly used in displays or lighting, occurs due to coupling excited two-level systems (TLS) to the vacuum modes of the electromagnetic field, effectively stimulated by its zero-point fluctuations. In 1954, R. H. Dicke predicted<sup>18</sup> that an ensemble of  $N$  identical TLS confined in a volume smaller than  $\sim \lambda^3$  ( $\lambda$  is the corresponding emission wavelength of the TLS) can exhibit coherent and cooperative spontaneous emission. This so-called superradiant emission results from the coherent coupling between individual TLS through the common vacuum modes, effectively leading to a single giant emitting dipole from all participating TLS. Superradiant emission has been observed in distinctly different physical systems, such as molecular aggregates and crystals<sup>19</sup>, nitrogen vacancy centres in diamond<sup>20</sup> and epitaxially grown quantum dots<sup>21</sup>. In the case when the excited TLS are initially fully uncorrelated, the coherence can be established only through spontaneously triggered correlations due to quantum fluctuations rather than by coherent excitation. When this occurs, a so-called superfluorescent (SF) pulse is emitted<sup>1</sup> (Figure 1, illustrated for the present study). Both superradiant emission and coherent SF bursts are characterized by an accelerated radiative decay time  $\tau_{\text{SF}} \sim \tau_{\text{SE}}/N$ , where the exponential decay time  $\tau_{\text{SE}}$  of the uncoupled TLS is shortened by the number of coupled emitters  $N$ . In addition, SF exhibits the following fundamental signatures, which magnitudes are also dependent on the excitation density: (i) a delay or build-up time  $\tau_{\text{D}} \sim \ln(N)/N$  during which the emitters couple and phase-synchronize to each other, and which corresponds to the time delay between the excitation and onset of the cooperative emission (Figure 1) and (ii) coherent Rabi-type oscillations in the time domain due to the strong light–matter interaction, known as Burnham–Chiao ringing<sup>14,22</sup>.

SF was first observed in a dense gas of hydrogen fluoride<sup>2</sup>, followed by a limited number of solid-state systems, such as CuCl nanocrystals (NCs) formed in a NaCl matrix<sup>4</sup>, KCl crystals doped with peroxide anions ( $O_2^-$ ) (ref.<sup>3</sup>), and some select semiconductor crystals (ZnTe and InGaAs/GaAs multi-quantum wells)<sup>5,6</sup>. Practical implementation of such an enhanced radiative property is a persistent challenge. Besides stringent requirements for the



emissive material (e.g., high oscillator strength, small inhomogeneous line-broadening, small exciton dephasing), equally important are structural, optical and device engineerability. Colloidal semiconductor NCs, also known as colloidal quantum dots (QDs), could fill this gap as they are structurally and optically versatile, and highly suited for the entire visible spectral range. While they are actively pursued for photonic applications<sup>8,9,23</sup>, they have not been reported to exhibit SF.

Here, we use colloidal NCs of caesium lead halide perovskites ( $\text{CsPbX}_3$ ,  $\text{X} = \text{Cl, Br}$ ) that can be synthesized with narrow size dispersion and are known to exhibit moderate quantum confinement effects, resulting in narrow-band emission combined with exceptionally large oscillator strength from a bright triplet state<sup>10,11,24</sup>. In order to foster cooperative behaviour, we employ structurally well-defined, long-range ordered, and densely packed arrays of such NCs, known as superlattices, produced by means of solvent-drying-induced spontaneous assembly<sup>25-28</sup>. Similarly, regular arrays of II-VI semiconductor NCs have been used to obtain collective effects in the electronic domain, *i.e.*, band-like transport<sup>15</sup>. Figure 2a outlines the superlattice formation (see also Methods), using a solution of highly monodispersed  $\text{CsPbBr}_3$  NCs with a mean size of 9.5 nm and standard size-deviation of less than 5% (Extended Data Figure 1). In the self-assembly process, cubic individual superlattice domains are formed (*i.e.*, supercrystals), each consisting of up to several millions of NCs. Optical microscopy (Figure 2c) reveals superlattices with a lateral size of up to 5  $\mu\text{m}$ , randomly distributed in a uniform film on a  $5 \times 7$  mm sample (Figure 2d). Transmission electron microscopy confirms that highly ordered superlattices consist of well-separated individual NCs (Figure 2e and Extended Data Figure 2). More details of the self-assembly process are reported in the Methods section.

Figure 3a displays the photoluminescence (PL) spectrum of a single  $\text{CsPbBr}_3$  superlattice (excited at 3.06 eV) exhibiting two emission peaks. This and all other optical measurements were performed at a temperature of 6 K in vacuum or Helium atmosphere (see Methods for details). The high-energy emission peak coincides with the centre energy of the disordered dense film of  $\text{CsPbBr}_3$  NCs (glassy state) and is therefore assigned to non-coupled QDs. In addition, a narrow, red-shifted emission peak appears in superlattices, which we assign to the emission of coupled QDs, which is best fitted with a Lorentzian (full width at half maximum,  $\text{FWHM}_{\text{coupled}} = 11$  meV). The peaks of the uncoupled QDs in a superlattice and

95 in the glassy films are best fitted with a Gaussian, as expected for disordered ensembles. The  
96 width of the uncoupled QDs ( $\text{FWHM}_{\text{uncoupled}} = 55 \text{ meV}$ ) is slightly broader than the one of the  
97 amorphous film ( $\text{FWHM}_{\text{amorphous}} = 35 \text{ meV}$ ), which can be explained assuming that the more  
98 “identical QDs” within the superlattice are now forming the peak of coupled QDs while the  
99 remaining uncoupled ones appear more disordered than the inhomogeneous energy  
100 distribution of the primary QD material. We can exclude that the red-shifted feature, which is  
101 at  $\sim 70 \text{ meV}$  lower energy than the uncoupled QD emission, originates from the emission from  
102 trions, bi-excitons or multi-excitons, because their energy shifts reportedly are  $10\text{--}20 \text{ meV}$   
103 (refs. <sup>11,12</sup>), and these would be observable in the disordered ensemble, too. The number and  
104 interaction strength of coupled QDs determine the magnitude of the energetic shift. Statistics  
105 from 10 superlattices from different samples give an average static red-shift of  $(64 \pm 6) \text{ meV}$ ,  
106 average  $\text{FWHM}_{\text{coupled}} = (15 \pm 4) \text{ meV}$  and average  $\text{FWHM}_{\text{uncoupled}} = (49 \pm 21) \text{ meV}$ . In most  
107 superlattices, we observe a sub-structure in this red-shifted emission band, which we attribute  
108 to the presence of several, slightly different independent domains within the same individual  
109 superlattice.

110 A central feature of the cooperative emission is the modification of the radiative  
111 lifetime<sup>18</sup>, as demonstrated experimentally with several quantum emitters<sup>6,20,21</sup>. In time-  
112 resolved PL decay measurements, at a very low excitation fluence ( $5 \text{ nJ/cm}^2$ ), we do not  
113 observe a significant modification of the decay of the coupled QD emission compared to the  
114 uncoupled QD emission (Figure 3b inset). The absence of accelerated emission at vanishing  
115 excitation density and the presence of the red-shifted feature also in PL excitation scans  
116 (Extended Data Figure 3) corroborates that the static  $\sim 70 \text{ meV}$  red-shift originates from  
117 incoherent coupling of the QDs in the ground state, similar to various molecular aggregates<sup>19</sup>.  
118 Already at a slightly higher excitation density, we observe an accelerated PL decay of the  
119 coupled QD emission peak in comparison to the PL decay of uncoupled QDs with  $1/e$  decay  
120 times of  $\tau_{\text{SF}} = 148 \text{ ps}$  and  $\tau_{\text{QD}} = 400 \text{ ps}$ , respectively, for an excitation density of  $500 \text{ nJ/cm}^2$   
121 per pulse (Figure 3b). In contrast to the predominantly mono-exponential decay of the  
122 uncoupled QDs, this SF emission decay is approximated well by a stretched exponential<sup>29</sup>  
123 (see Methods section), because the number of excited coupled emitters, and therefore the  
124 emission acceleration, varies during the decay. Furthermore, in contrast to the uncoupled  
125 QDs, the SF decay time is strongly dependent on excitation power (inset Figure 3b) because

126 it scales with the coupling strength among the QDs, given by the intensity in the common  
127 light-field that effectively corresponds to a change in the number of coherently coupled QDs.  
128 When the spectrally and temporally integrated emission is fitted with a power law, we obtain  
129 an exponent of 1 (Extended Data Figure 4), indicating that excitation density-dependent non-  
130 radiative decay channels (e.g. Auger recombination) are absent. Notably, no threshold  
131 behaviour as for amplified spontaneous emission (ASE) is observed.

132 The cooperative emission process strongly influences the coherence of the emitted  
133 light. First-order correlation measurements of each of the two emission peaks by means of a  
134 Michelson interferometer allow us to monitor the interference pattern and therefore the phase  
135 coherence time (Figure 4a). The emission band of the uncoupled QDs exhibits 38 fs  
136 coherence time, best fitted with a Gaussian decay (Figure 4a, upper graph), typical of  
137 incoherent (thermal) light sources. The emission from the coherently coupled QDs (Figure 4a,  
138 lower graph) exhibits a much longer coherence time with an exponential decay of 140 fs. For  
139 some superlattices, a Gaussian decay is observed (Extended Data Figure 5a), which might  
140 be attributed to number fluctuations within the coherent SF state<sup>30</sup>.

141 Second-order coherence of the emitted light is evinced by the statistics of the photon  
142 arrival time on a detector<sup>31</sup>. Typical coherent light, as from a laser, shows a random  
143 distribution (Poissonian) of photon arrival times, while a single TLS exhibits photon  
144 antibunching (sub-Poissonian distribution). In contrast, the cooperative emission from coupled  
145 QDs leads to coherent multi-photon emission bursts. Figure 4 reports the second-order  
146 correlation function,  $g^{(2)}(\tau) = \frac{\langle I(t)I(t+\tau) \rangle}{\langle I(t) \rangle^2}$  for both PL emission bands, where  $I(t)$  is the signal  
147 intensity at time  $t$ . For the uncoupled QD emission (Figure 4b, upper graph), a flat  $g^{(2)}(\tau) = 1$   
148 is observed because the experimental temporal resolution (40 ps) is insufficient to resolve the  
149 expected thermal bunching. The SF emission band, however, shows pronounced photon  
150 bunching (Figure 4b, lower graph) because the coherent coupling leads to the correlated  
151 emission of multiple photons within a short time interval. Photon bunching is only observable  
152 in superlattices with single or a few SF domains, *i.e.*, where no sub-structure is visible in the  
153 red-shifted emission band, because spectrally overlapping uncorrelated aggregated domains  
154 within the same superlattice reduce the bunching peak's visibility, as predicted by theory<sup>32</sup>.  
155 Yet, it is a robust effect that is observed with pulsed excitation and for mixed-halide

(CsPbBr<sub>2</sub>Cl, emitting at higher energies) QD superlattices, too (see Extended Data Figure 5b and 6b, respectively). Remarkably, some superlattices with supposedly well-isolated coherently coupled QDs exhibit  $g^{(2)}(\tau) > 2$  (inset Figure 4), similar to superthermal emission<sup>31</sup>. The exponential decay time of the second-order correlation is of the order of the radiative decay of the SF emission for low excitation densities ( $\tau_{g^{(2)}} = 224$  ps).

Very distinct characteristics of SF emission concern the time evolution of the emitted light under strong driving conditions. Figure 5a shows a streak camera image acquired at an excitation density of 600  $\mu\text{J}/\text{cm}^2$ , where in addition to a drastically shortened radiative decay, a finite rise time and subsequent oscillations of the emission are observed. Quantitative analysis on spectrally integrated PL decay traces for various excitation power densities is shown in Figure 5b (for details see Methods). As a function of the excitation density, the decay time shortens to 14 ps (Figure 5c, upper panel). From this decay shortening, which is an order of magnitude stronger than reported for the collective emission from other QD systems<sup>4,21</sup>, we can estimate an average number of coherently coupled QDs to be  $N \sim 28$ . This is only an effective value and a conservative estimate, because the energetic disorder of the QD emission energies ( $\text{FWHM}_{\text{coupled}} = 11$  meV) still exceeds significantly the emission peak width of individual QDs (typically  $\text{FWHM} \sim 1$  meV, ref. <sup>11</sup>) and thereby effectively reduces the SF coupling<sup>33</sup>. The SF emission experiences a dynamical red-shift of up to 15 meV due to renormalization of the emission energy from the coherent coupling<sup>7</sup>, which decreases in the course of the decay as the number of excitations reduces (Extended Data Figure 7). The peak intensity increases super-linearly over three orders of magnitude (Figure 5c, middle panel), according to a power-law dependence with an exponent of  $\alpha = 1.5 \pm 0.1$ , deviating from the theoretically expected value of  $\alpha = 2$  (ref. <sup>7</sup>), presumably due to saturation effects<sup>5</sup>. Nevertheless, no significant quenching effects of the emission for high excitation powers were found, verifying that the decay remains essentially radiative (Extended Data Figure 4d). Furthermore, a shortening of the SF delay time ( $\tau_D$ ), after which the photon burst is emitted, is observed (Figure 5c, bottom panel). This characteristic of SF is a consequence of the time it takes for phase-locking the individual dipoles and scales with the number  $N$  of excited coupled QDs according to  $\tau_D \sim \frac{\log(N)}{N}$  (see Methods section).

As SF crucially depends on low decoherence and low inhomogeneous spread, it should be noted that SF coupling is strongly affected by the environment around the QDs (number of free ligands), the superlattice assembly, and by the quality of the QDs themselves. Thus, while a large fraction of the superlattices displays a red-shifted peak from the coupled QD emission, the amount of photon-bunching and Burnham–Chiao ringing varied from superlattice to superlattice. However, experiments employing different batches of NCs and superlattice assemblies of CsPbBr<sub>3</sub> and CsPbBr<sub>2</sub>Cl NCs (see Extended Data Figures 6-9) were consistently reproducible, but further optimization of the synthesis and assembly is likely to improve the yield of SF domains. It is important to note that experiments on control samples with diluted, uncoupled QDs under similar excitation conditions do not show any of these signatures of SF (Extended Data Figure 10), proving that it is a genuine multi-particle effect.

Our measurements reveal that coherent SF coupling can be achieved in long-range ordered self-assembled superlattices of fully inorganic CsPbX<sub>3</sub> perovskite NCs, resulting in strong emission bursts. Colloidal NCs and their assemblies have proven to be excellent building blocks for a large variety of opto-electronic devices, and these cooperative effects now allow modification of the opto-electronic properties beyond what is possible on the individual QD level with chemical engineering approaches. This opens up new opportunities for high-brightness and multi-photon quantum light sources, and could enable the exploitation of cooperative effects for long-range quantum transport and ultra-narrow tuneable lasers.

## References

- 1 Bonifacio, R. & Lugiato, L. A. Cooperative radiation processes in two-level systems: Superfluorescence. *Physical Review A* **11**, 1507-1521 (1975).
- 2 Skribanowitz, N., Herman, I. P., MacGillivray, J. C. & Feld, M. S. Observation of Dicke Superradiance in Optically Pumped HF Gas. *Physical Review Letters* **30**, 309-312 (1973).
- 3 Malcuit, M. S., Maki, J. J., Simkin, D. J. & Boyd, R. W. Transition from superfluorescence to amplified spontaneous emission. *Physical Review Letters* **59**, 1189-1192 (1987).
- 4 Miyajima, K., Kagotani, Y., Saito, S., Ashida, M. & Itoh, T. Superfluorescent pulsed emission from biexcitons in an ensemble of semiconductor quantum dots. *Journal of Physics: Condensed Matter* **21**, 195802 (2009).
- 5 Dai, D. C. & Monkman, A. P. Observation of superfluorescence from a quantum ensemble of coherent excitons in a ZnTe crystal: Evidence for spontaneous Bose-Einstein condensation of excitons. *Physical Review B* **84**, 115206 (2011).

219 6 Noe II, G. T. *et al.* Giant superfluorescent bursts from a semiconductor magneto-plasma. *Nature Physics*  
220 **8**, 219-224 (2012).

221 7 Cong, K. *et al.* Dicke superradiance in solids. *J. Opt. Soc. Am. B* **33**, C80-C101 (2016).

222 8 Talapin, D. V., Lee, J.-S., Kovalenko, M. V. & Shevchenko, E. V. Prospects of Colloidal Nanocrystals for  
223 Electronic and Optoelectronic Applications. *Chemical Reviews* **110**, 389-458 (2010).

224 9 Kovalenko, M. V. *et al.* Prospects of Nanoscience with Nanocrystals. *ACS Nano* **9**, 1012-1057 (2015).

225 10 Protesescu, L. *et al.* Nanocrystals of Cesium Lead Halide Perovskites (CsPbX<sub>3</sub>, X = Cl, Br, and I): Novel  
226 Optoelectronic Materials Showing Bright Emission with Wide Color Gamut. *Nano Letters* **15**, 3692-3696  
227 (2015).

228 11 Rainò, G. *et al.* Single Cesium Lead Halide Perovskite Nanocrystals at Low Temperature: Fast Single-  
229 Photon Emission, Reduced Blinking, and Exciton Fine Structure. *ACS Nano* **10**, 2485-2490 (2016).

230 12 Fu, M. *et al.* Neutral and Charged Exciton Fine Structure in Single Lead Halide Perovskite Nanocrystals  
231 Revealed by Magneto-optical Spectroscopy. *Nano Letters* **17**, 2895-2901 (2017).

232 13 Kovalenko, M. V., Protesescu, L. & Bodnarchuk, M. I. Properties and potential optoelectronic  
233 applications of lead halide perovskite nanocrystals. *Science* **358**, 745-750 (2017).

234 14 Burnham, D. C. & Chiao, R. Y. Coherent Resonance Fluorescence Excited by Short Light Pulses. *Physical*  
235 *Review* **188**, 667-675 (1969).

236 15 Kagan, C. R. & Murray, C. B. Charge transport in strongly coupled quantum dot solids. *Nature*  
237 *Nanotechnology* **10**, 1013-1026 (2015).

238 16 Afek, I., Ambar, O. & Silberberg, Y. High-NOON States by Mixing Quantum and Classical Light. *Science*  
239 **328**, 879 (2010).

240 17 Munoz, C. S. *et al.* Emitters of N-photon bundles. *Nature Photonics* **8**, 550-555 (2014).

241 18 Dicke, R. H. Coherence in Spontaneous Radiation Processes. *Physical Review* **93**, 99-110 (1954).

242 19 Spano, F. C. The Spectral Signatures of Frenkel Polarons in H- and J-Aggregates. *Accounts of Chemical*  
243 *Research* **43**, 429-439 (2010).

244 20 Bradac, C. *et al.* Room-temperature spontaneous superradiance from single diamond nanocrystals.  
245 *Nature Communications* **8**, 1205 (2017).

246 21 Scheibner, M. *et al.* Superradiance of quantum dots. *Nature Physics* **3**, 106-110 (2007).

247 22 Heinzen, D. J., Thomas, J. E. & Feld, M. S. Coherent Ringing in Superfluorescence. *Physical Review*  
248 *Letters* **54**, 677-680 (1985).

249 23 Shirasaki, Y., Supran, G. J., Bawendi, M. G. & Bulović, V. Emergence of colloidal quantum-dot light-  
250 emitting technologies. *Nature Photonics* **7**, 13 (2012).

251 24 Becker, M. A. *et al.* Bright triplet excitons in caesium lead halide perovskites. *Nature* **553**, 189 (2018).

252 25 Boles, M. A., Engel, M. & Talapin, D. V. Self-Assembly of Colloidal Nanocrystals: From Intricate  
253 Structures to Functional Materials. *Chemical Reviews* **116**, 11220-11289 (2016).

254 26 Murray, C. B., Kagan, C. R. & Bawendi, M. G. Synthesis and Characterization of Monodisperse  
255 Nanocrystals and Close-Packed Nanocrystal Assemblies. *Annual Review of Materials Science* **30**, 545-  
256 610 (2000).

257 27 Geuchies, J. J. *et al.* In situ study of the formation mechanism of two-dimensional superlattices from  
258 PbSe nanocrystals. *Nature Materials* **15**, 1248 (2016).

259 28 Nagaoka, Y. *et al.* Nanocube Superlattices of Cesium Lead Bromide Perovskites and Pressure-Induced  
260 Phase Transformations at Atomic and Mesoscale Levels. *Advanced Materials* **29**, 1606666 (2017).

261 29 Temnov, V. V. & Woggon, U. Superradiance and Subradiance in an Inhomogeneously Broadened  
262 Ensemble of Two-Level Systems Coupled to a Low-Q Cavity. *Physical Review Letters* **95**, 243602 (2005).

263 30 Whittaker, D. M. & Eastham, P. R. Coherence properties of the microcavity polariton condensate.  
264 *Europhysics Letters* **87**, 27002 (2009).

265 31 Jahnke, F. *et al.* Giant photon bunching, superradiant pulse emission and excitation trapping in  
266 quantum-dot nanolasers. *Nature Communications* **7**, 11540 (2016).

- 32 Temnov, V. V. & Woggon, U. Photon statistics in the cooperative spontaneous emission. *Optics Express*  
 17, 5774 (2009).  
 33 Ishikawa, A., Miyajima, K., Ashida, M., Itoh, T. & Ishihara, H. Theory of Superfluorescence in Highly  
 Inhomogeneous Quantum Systems. *Journal of the Physical Society of Japan* **85**, 034703 (2016).

## Main Figure Legends

**Figure 1 | Schematic of the build-up process of SF.** An initially uncorrelated ensemble of TLS (randomly oriented green arrows) is excited by a light pulse (blue arrow). After time  $\tau_D$  their phases are synchronized (aligned green arrows) such that they cooperatively emit a SF light pulse (red arrow). Grey cubes represent long-range ordered self-assembled superlattices.

**Figure 2 | Formation of CsPbX<sub>3</sub> (X = Cl, Br) NC superlattices by drying-mediated self-assembly.** **a**, Illustration of the assembly process. **b**, High-resolution scanning transmission electron microscopy image (HAADF–STEM) of a single CsPbBr<sub>3</sub> NC. **c**, Optical microscope image and **d**, photograph (under UV light) of a layer of micron-sized, three-dimensional, cubic-shaped NC superlattices. **e**, HAADF–STEM image of a single superlattice of CsPbBr<sub>3</sub> NCs. The cubic shape of the individual perovskite NC building blocks is translated into the symmetry of the superlattice (simple cubic packing). The inset shows a zoom-in where the individual NCs are visible.

**Figure 3 | Optical properties of CsPbBr<sub>3</sub> QD superlattices.** **a**, PL spectrum of a single CsPbBr<sub>3</sub> superlattice (black solid line). The high-energy band is assigned to the emission of uncoupled QDs. The low-energy band is the result of the emission of coupled QDs and is not present in glassy films of NCs (green solid line). The shaded areas are fits to the data (see main text). **b**, Time-resolved PL decay of the two emission bands at 500 nJ/cm<sup>2</sup> excitation density after applying suitable spectral filters to separate the two components. With increasing excitation density, the decay from the coherently coupled QDs is significantly faster than from the uncoupled ones. The inset shows the power-dependence of the 1/e-decay times of both components.

**Figure 4 | First- and second-order coherence properties of CsPbBr<sub>3</sub> QD superlattices.** **a**, First-order correlation of the two emission bands as obtained from the interference fringe visibility using a Michelson interferometer. The high-energy band of the uncoupled QDs has a very short phase coherence time (<40 fs, upper graph), whereas the red-shifted band from the coupled QDs is characterized by much longer phase coherence (140 fs, lower graph). The solid lines are fits to the data (see text). The inset shows an example of the real space interferogram. **b**, Second-order correlation function,  $g^{(2)}(\tau)$ , obtained with a Hanbury–Brown and Twiss setup in start–stop configuration. For the high-energy band (upper graph), a flat profile with  $g^{(2)}(\tau) = 1$  is observed. The red-shifted emission band (lower graph) from the SF emission displays a pronounced bunching peak, characteristic of the correlated emission during a photon burst. The data are fitted to the function  $g^{(2)}(\tau) = 1 + A \cdot \exp(-(|\tau - \tau_0|/\tau_c))$  (solid lines). The inset shows an example of superbunching with  $g^{(2)}(0) > 2$  from a single superlattice.

**Figure 5 | Burnham–Chiao ringing behaviour of CsPbBr<sub>3</sub> QD superlattices.** **a**, Streak camera image of SF dynamics obtained with high excitation density of 600  $\mu\text{J}/\text{cm}^2$ . **b**, Extracted time-resolved emission intensity traces for five different excitation powers. Solid red lines are weighted best-fits to a model that employs a bi-exponential decay function with damped oscillations. **c**, *Top*: Effective SF decay (blue circles) as a function of the excitation power density fitted according to the SF model (solid blue line). *Middle*: Red circles represent the peak SF emission intensity that increases super-linearly with excitation power, corresponding to a power-law dependence with an exponent  $\alpha = 1.5 \pm 0.1$  (solid dark-red line). *Bottom*: The extracted delay time  $\tau_D$  (green



313 circles) decreases at high excitation power due to the increased interaction among the emitters. The green solid  
314 line is the best fit according the model described in the Methods section. The error bars represent the  
315 parameters' fit uncertainty.

316

317

## METHODS

**Synthesis of CsPbBr<sub>3</sub> nanocrystals.** In a 25 ml three-necked flask, PbBr<sub>2</sub> (69 mg, 0.188 mmol, Aldrich, 99%) was suspended in octadecene (5 ml), dried at 100°C for 30 min, and mixed with oleic acid (0.5 ml, vacuum-dried at 100°C) and oleylamine (0.5 ml vacuum-dried at 100°C). When PbBr<sub>2</sub> was dissolved, the reaction mixture was heated up to 180°C and preheated caesium oleate in octadecene (0.4 ml, 0.125 M) was injected. The reaction mixture was cooled immediately with an ice bath to room temperature.

**Synthesis of CsPbBr<sub>2</sub>Cl nanocrystals.** In a 25 ml three-necked flask, PbBr<sub>2</sub> (45 mg, 0.12 mmol, Aldrich, 99%), PbCl<sub>2</sub> (18 mg, 0.064 mmol, ABCR) and 1 ml trioctylphosphine (Strem, 97%) was suspended in octadecene (5 ml), dried at 100°C for 30 min, and mixed with oleic acid (0.5 ml, vacuum-dried at 100°C) and oleylamine (0.5 ml vacuum-dried at 100°C). When PbCl<sub>2</sub> and PbBr<sub>2</sub> were dissolved, the reaction mixture was heated up to 180°C and preheated caesium oleate in octadecene (0.4 ml, 0.125 M) was injected. The reaction mixture was cooled immediately with an ice bath to room temperature.

**Purification and size-selection of CsPbX<sub>3</sub> (X = Cl, Br) nanocrystals.** A critical factor for self-assembly of cubic-shaped CsPbX<sub>3</sub> NCs is to start with an initially high level of monodispersity. The crude solution was centrifuged at 12100 rpm for 5 min, following which the supernatant was discarded, and the precipitate was dissolved in 300 µl hexane. The hexane solution was centrifuged again and the precipitate was discarded. The supernatant was diluted two times and used for further purification. Subsequently, two methods of purification of the NCs were applied: (a) 50 µl hexane, 0.6 µl oleic acid, and 0.6 µl oleylamine were added to 50 µl NCs in hexane. The colloid was destabilized by adding 50 µl acetone, followed by centrifuging and dispersing the NCs in 300 µl toluene. This solution was used further for the preparation of the 3D-superlattices. (b) 50 µl hexane and 100 µl toluene were added to 50 µl NCs in hexane. The colloid was destabilized by adding 50 µl acetonitrile, followed by centrifuging and dispersing the NCs in 300 µl toluene. This solution was used further for the preparation of the 3D-superlattices.

**Preparation of 3D-superlattices.** CsPbX<sub>3</sub> NC superlattices were prepared on glass or on 5 × 7 mm silicon substrates. Shortly before the self-assembly process, the silicon substrate was dipped into 4% solution of HF in water for 1 min, followed by washing with water. In a typical assembly process, the substrate was placed in a 10 × 10 × 10 mm Teflon well and 10 µl of purified NCs in toluene were spread onto the substrate. The well was covered with a glass

slide and the toluene was then allowed to evaporate slowly. 3D-superlattices of CsPbBr<sub>3</sub> NCs were formed upon complete evaporation of the toluene. Typical lateral dimensions of individual superlattices ranged from 1 to 10  $\mu\text{m}$  wherein some of them arrange into clusters of several superlattices and others remain spatially well-isolated so that PL measurements can be performed on an individual superlattice. More intense purification or greater polydispersity of NCs led to disordered or 2D assemblies (glassy films). Furthermore, the formation of NC superlattices can serve to further narrow the size distribution and shape uniformity within the ensemble (with smaller or larger NCs being repelled from the NC domain), especially in the case of simple cubic packing of cubes, which is particularly intolerant to size and shape variations.

**Optical spectroscopy.** All measurements were performed at cryogenic temperatures (6 K). For PL, time-resolved PL, and second-order photon-correlation measurements on single superlattices, the sample was mounted in an evacuated liquid-helium flow cryostat on xyz positioning stages and excited with a fibre-coupled excitation laser at an energy of 3.06 eV, either in continuous wave mode or pulsed mode with 40 MHz repetition rate (pulse duration 50 ps). The excitation laser was filtered with a short-pass filter and directed towards the long-working distance 100 $\times$  microscope objective (numerical aperture  $NA = 0.7$ ) by a dichroic beam splitter, resulting in a nearly Gaussian-shaped excitation spot with  $1/e^2$  radius of 1.4  $\mu\text{m}$ . The emission was collected via the same microscope objective and filtered using a tuneable bandpass filter. For PL measurements, the collected light was then dispersed by a 300 lines/mm grating inside a 750 mm monochromator and detected by an EMCCD camera. For measurements of the PL decay, we filtered the emission with a tuneable band-pass (FWHM = 15 nm) and recorded the decay with an avalanche photo diode single photon detector with a time resolution of 30 ps connected to a time-correlated single-photon-counting system. The photon correlation was recorded using a similar setup with two detectors in a Hanbury–Brown–Twiss setup configuration.

To record streak camera images and first-order coherence measurements, we excited the sample, which was mounted in an exchange-gas cryostat at 6 K, with a frequency-doubled regenerative amplifier seeded with a mode-locked Ti:sapphire laser with a pulse duration of 100–200 fs and a repetition rate of 1 kHz at 3.1 eV. For both excitation and detection, we used an 80 mm lens ( $NA = 0.013$  after iris), resulting in an excitation spot area of  $20 \times 40 \mu\text{m}$ .

381 The recorded PL was dispersed by a grating with 150 lines/mm in a 300 mm spectrograph  
382 and detected with a streak camera with a nominal time resolution of 2 ps and an instrument  
383 response function FWHM of 4 ps (see Extended Data Figure 10). First-order coherence  
384 measurements were performed using a Michelson interferometer. Here a non-polarizing  
385 beam splitter is used to split and recombine the light in the two interferometer arms, with one  
386 arm including a retroreflector on a delay stage with 100 nm step resolution. A tuneable band-  
387 pass filter is applied to select the emission from either the coupled or the uncoupled QDs. The  
388 interferogram was recorded as real-space images of the recombined and focused detection  
389 beams on a camera.

390 **Optical properties of superfluorescence, superradiance, and subradiance.** As shown in  
391 Figure 3b, we observed that the PL decay of the SF state is initially very fast and cannot be  
392 described with a single exponential because the decay rate is dependent on the number of  
393 excited TLS,  $\Gamma(N) \sim N$ , and therefore decreases during the decay. Consequently, the SF  
394 decay rate should converge towards the decay rate of the uncoupled nanocrystals. However,  
395 we observe that the SF decay trace crosses the bi-exponential PL decay of the uncoupled  
396 QDs after 97% of the photons are emitted due to long decay components. These long decay  
397 components might originate from coupled QDs where the individual dipoles are out of phase  
398 and interfere destructively, known as subradiance (SBR)<sup>29,34</sup>. In ensembles with  
399 inhomogeneously broadened PL, SF and subradiant states can coexist, and we find a good  
400 agreement of the predicted excited state population with the measured PL decay<sup>35</sup>.

401 An out-of-phase coupling amongst the QDs is expected to result in a higher photon energy of  
402 the subradiant state compared to the SF state. In Extended Data Figure 7 and Extended Data  
403 Figure 9, we provide an analysis of the dynamical energy shift observed at high excitation  
404 power density for CsPbBr<sub>3</sub> and CsPbBr<sub>2</sub>Cl QD superlattices, respectively. Examples of  
405 emission spectra at different times are reported in Extended Data Figure 7a and Extended  
406 Data Figure 9a for the respective QD halide compositions. In Extended Data Figure 7b and  
407 Extended Data Figure 9b, we plot the fitted centre photon energy of time-sliced PL spectra (2  
408 ps bin) as a function of the fitted peak area (*i.e.*, the time-dependent emission intensity), as  
409 obtained from excitation power-dependent streak camera images, again for both, CsPbBr<sub>3</sub>  
410 and CsPbBr<sub>2</sub>Cl QD superlattices. This effectively shows the energetic shift of the SF state as  
411 a function of its occupation, with the different curves representing different initial excitation  
412 powers. The green arrows indicate the time sequence of the individual analysed spectral

traces. By increasing the excitation power, we observe that the initial dynamical red-shift is the largest for the highest excitation power, as is expected from its relationship to the number of excited coupled QDs. Hence, when the number of excited coupled QDs decreases during the decay process, the emission energy blue-shifts to higher energy, as can be seen in Extended Data Figures 7c and 9c where the fitted centre photon energy is plotted as a function of time. We observe the most pronounced energetic blue-shift for the highest excitation power, resulting in a final emission with a photon energy that has been boosted incrementally more in comparison to the blue-shift for low excitation power, which is another indication of the presence of subradiant states that emit at higher energies. For high excitation power, the SF state becomes depopulated much faster since more QDs are coupled simultaneously. Then, at long timescales after the initial decay, the percentage of subradiant states becomes dominant, resulting in a blue-shift of the PL emission.

**Superfluorescence fit model.** SF decay traces as in Figure 3b cannot be fitted well with mono- or bi-exponential functions because the decay rate is proportional to the number of excited coupled QDs  $\Gamma(N) \sim N$ , which also decays over time. Furthermore, the resulting characteristic decay neither exactly follows stretched-exponential nor a power-law dependence<sup>36</sup>, whereas the PL decay of the uncoupled QDs is well described by a bi-exponential behaviour, where the initial fast decay  $\tau_{\text{QD}} = 349.8 \pm 0.4$  ps accounts for over 96% the total emitted photons. Nevertheless, we found that the best approximate fit to the SF decay trace is the Kohlrausch stretched-exponential decay model  $\frac{f(t)}{f(0)} = \exp[-(\Gamma_{\text{stretched}} \cdot t)^\beta]$ , where  $\Gamma_{\text{stretched}}$  is the average decay time and  $\beta \in [0,1]$  is the stretch parameter, which represents the distribution of decay rates<sup>37</sup>. Using this model to fit the SF decay curve, we obtain an average decay time  $\tau_{\text{stretched}} = 40.4 \pm 0.5$  ps and a stretch parameter  $\beta = 0.457 \pm 0.002$ .

At a high excitation density, as shown in Figure 5b for CsPbBr<sub>3</sub> QD superlattices and in Extended Data Figure 8b for CsPbBr<sub>2</sub>Cl QD superlattices, we observe oscillations in the decay. To model the SF decay with this characteristic ringing behaviour, we used a decay model consisting of a bi-exponential decay that is multiplied by a damped oscillating term  $1 + B \cdot \exp(-\gamma_{\text{Damp}} t) \cdot \cos(\omega t + \phi_0)$ . Furthermore, for the rising edge of the emitted pulse we

442 take into account a Gaussian rise term  $\sim \exp[-(\frac{t-\tau_D}{\tau_{\text{rise}}})^2]$ , such that the complete fit function is  
 443 given by (ref.<sup>38</sup>):

$$f(t) = \sum_{n=1,2} A_n \cdot \exp\left(\frac{\tau_{\text{rise}}^2}{4\tau_n^2} - \frac{t - \tau_D}{\tau_n}\right) \cdot \left[ \frac{1}{2} (1 + B \cdot \exp(-\gamma_{\text{Damp}}(t - \tau_D)) \cdot \cos(\omega(t - \tau_D) + \phi_0)) \cdot \left[ 1 + \text{erf}\left(\frac{t - \tau_D}{\tau_{\text{rise}}} - \frac{\tau_{\text{rise}}}{2\tau_n}\right) \right] \right]$$

444

445 Here,  $A_n$  are the amplitudes of the exponential decay with the corresponding decay time  
 446 constants,  $\tau_n$ . Both the fast decay time and the long decay time component (Extended Data  
 447 Figure 7d for CsPbBr<sub>3</sub> QD superlattices and Extended Data Figure 9d for CsPbBr<sub>2</sub>Cl QD  
 448 superlattices) decrease upon increasing the excitation density, whereas the rise time,  
 449  $\tau_{\text{rise}} = 2.4 \pm 0.3$  ps for CsPbBr<sub>3</sub> QD superlattices ( $\tau_{\text{rise}} = 3.4 \pm 1.0$  ps for CsPbBr<sub>2</sub>Cl QD  
 450 superlattices), stays approximately constant (probably clamped by the time resolution of the  
 451 setup). In the upper panel of Figure 5c, we plot the power-dependent effective decay time  
 452  $\tau_{\text{SF}} = \frac{A_1\tau_1 + A_2\tau_2}{A_1 + A_2}$  for CsPbBr<sub>3</sub> QD superlattices, where  $\tau_1, \tau_2$  are the decay times of the bi-  
 453 exponential fit and  $A_1, A_2$  the corresponding amplitudes, which was fitted with  $\tau_{\text{SF}}(P) = \frac{\tau_{\text{QD}}}{\zeta \cdot P + 1} +$   
 454  $y_0$ , with a fixed value of  $\tau_{\text{QD}} = 400$  ps, obtained from the time-resolved PL measurements of  
 455 uncoupled QDs and an additional offset  $y_0$  to account for effects like the finite time resolution.  
 456 We obtain good agreement with the expected behaviour ( $\tau_{\text{SF}} \sim \tau_{\text{QD}}/N$ ) for a value  $\zeta_{\text{CsPbBr}_3} =$   
 457  $0.29 \pm 0.04 \frac{\text{cm}^2}{\mu\text{J}}$ . In the lower panel of Figure 5c, we plot the delay time  $\tau_D$  for the CsPbBr<sub>3</sub> QD  
 458 superlattices as a function of the excitation power. In our analysis, the delay time is composed  
 459 of the actual delay time due to the SF build-up and a systematic, constant time-offset because  
 460 the absolute arrival time of the excitation pulse (which has a different wavelength than the  
 461 emission) at the sample cannot be measured reliably at the required precision from the streak  
 462 camera data. We observe a decrease in  $\tau_D$  of  $\sim 6$  ps when increasing the excitation density by  
 463 almost 2 orders of magnitude. We have fitted this behaviour with  $\tau_D = y_{\text{offset}} + A \cdot \ln(\zeta P_{\text{Exc}} +$   
 464  $1)/(\zeta P_{\text{Exc}} + 1)$  because we assume that  $\tau_D \sim \ln(N)/N$  and that the number of excited coupled

emitters  $N \sim \alpha P_{\text{Exc}} + 1$  is proportional to the excitation power. Herein, we use a fixed value  $\zeta_{\text{CsPbBr}_3} = 0.29 \pm 0.04 \frac{\text{cm}^2}{\mu\text{J}}$ , which we obtained from the fit of the effective decay in the upper panel of Figure 5c. The resulting fit agrees very well with the data. To obtain the absolute time delay, we subtracted the constant offset  $y_{\text{offset}}$  of the time-delay fit from the time-delay data points. SF occurs when  $\sqrt{\tau_{\text{SF}}\tau_{\text{D}}} < T_2^*$ , where  $T_2^*$  is the exciton pure dephasing time, whereas  $\sqrt{\tau_{\text{ASE}}\tau_{\text{D}}} > T_2^*$  signifies the amplified spontaneous emission (ASE) regime, when  $\tau_{\text{ASE}}$  is the decay time (ref. <sup>33</sup>). Considering that the coherence time  $T_2 < T_2^*$  extracted from the full-width at half-maximum of single QDs<sup>11</sup> is of the order of  $T_2 = 6.6$  ps, our measurements reveal a fast decay of  $\sim 14$  ps and a delay time of  $< 1$  ps which satisfies the criterion for the appearance of SF.

A similar analysis was performed on CsPbBr<sub>2</sub>Cl QD superlattices as shown in Extended Data Figure 8. In the upper panel of Extended Data Figure 8c we plot power-dependent effective decay time and fit the data with the same model as described above, using  $\tau_{\text{QD}} = 250$  ps and we obtain a value  $\zeta_{\text{CsPbBr}_2\text{Cl}} = 0.08 \pm 0.01 \frac{\text{cm}^2}{\mu\text{J}}$ . The peak intensity of the decay curves as a function of the excitation density is shown in the middle panel of the Extended Data Figure 8c, which increases super-linearly with a power-law dependence with an exponent  $\alpha_{\text{CsPbBr}_2\text{Cl}} = 1.3 \pm 0.1$ . Also the delay time decreases as a function of the excitation density as displayed in the lower panel of Extended Data Figure 8c and fit the data. Again, we fit the data using the same formula for  $\tau_{\text{D}}$  as described above with a fixed value  $\zeta_{\text{CsPbBr}_2\text{Cl}} = 0.08 \pm 0.01 \frac{\text{cm}^2}{\mu\text{J}}$  and obtain good agreement.

## Additional references

- 34 DeVoe, R. G. & Brewer, R. G. Observation of Superradiant and Subradiant Spontaneous Emission of Two Trapped Ions. *Physical Review Letters* **76**, 2049-2052 (1996).
- 35 Bienaimé, T., Piovella, N. & Kaiser, R. Controlled Dicke Subradiance from a Large Cloud of Two-Level Systems. *Physical Review Letters* **108**, 123602 (2012).
- 36 Guerin, W., Rouabah, M. T. & Kaiser, R. Light interacting with atomic ensembles: collective, cooperative and mesoscopic effects. *Journal of Modern Optics* **64**, 895-907 (2017).
- 37 van Driel, A. F. *et al.* Statistical analysis of time-resolved emission from ensembles of semiconductor quantum dots: Interpretation of exponential decay models. *Physical Review B* **75**, 035329 (2007).
- 38 Naeem, A. *et al.* Giant exciton oscillator strength and radiatively limited dephasing in two-dimensional platelets. *Physical Review B* **91**, 121302 (2015).



498

499

500 **Acknowledgements**

501 We thank D. J. Norris, C. Schwemmer, D. Urbonas, and F. Scafirimuto for helpful  
502 discussions. F. Krieg is acknowledged for providing additional samples for control  
503 experiments. M.A.B., M.V.K., T.S., R.F.M., and G.R. acknowledge the European Union's  
504 Horizon-2020 programme through the Marie-Sklodowska Curie ITN network PHONSI (H2020-  
505 MSCA-ITN-642656) and the Swiss State Secretariat for Education Research and Innovation  
506 (SERI). M.I.B. acknowledges financial support from the Swiss National Science Foundation  
507 (SNF Ambizione grant, Grant No. PZENP2\_154287). M.V.K. acknowledges financial support  
508 from the European Research Council under the European Union's Seventh Framework  
509 Program (FP/2007-2013) / ERC Grant Agreement No. 306733 (NANOSOLID Starting Grant).

510

511 **Author contributions**

512 The work originated from ongoing interactions between G.R., M.V.K, R.F.M., and T.S. M.I.B.  
513 prepared the samples and performed their structural characterization. G.R., M.A.B., and T.S.  
514 performed the optical experiments, interpreted the data with input from R.F.M. G.R. and  
515 M.A.B. wrote the manuscript with input from all the co-authors. R.F.M., M.V.K., and T.S.  
516 supervised the work.

517

518 **Author information**

519 Correspondence and requests for materials should be addressed to G.R. (rainog@ethz.ch),  
520 M.V.K. (mvkovalenko@ethz.ch), and T.S. (tof@zurich.ibm.com).

521

522 **Data availability.** The data that support the findings of this study are available from the  
523 corresponding authors upon reasonable request.

524

525 **The authors declare no competing interests.**

## Extended Data Figure Legends

**Extended Data Figure 1 | Quantitative analysis of CsPbBr<sub>3</sub> NC size distribution.** **a**, Low-resolution TEM image of the NC material which is used to prepare the superlattices. **b**, Histogram of NC sizes (of >100 NCs) as obtained from TEM image analysis. The solid line is a fit with a normal distribution.

**Extended Data Figure 2 | HAADF-STEM image of a single superlattice of CsPbBr<sub>3</sub> NCs.** Individual NCs (bright spots in the image) are well-resolved.

**Extended Data Figure 3 | PL excitation measurement of CsPbBr<sub>3</sub> QD superlattices.** Using a weak, tuneable excitation source, we plot the PL intensity (black circles) obtained at 2.30 eV photon energy as a function of excitation photon energy. The shaded areas are Gaussian peak fits. This shows that the coupled QD feature is also present in the absorption spectrum, in addition to the uncoupled QDs and more energetically higher states.

**Extended Data Figure 4 | Power dependent PL properties of CsPbBr<sub>3</sub> QD superlattices.** **a**, Colour-coded PL emission in the low-power excitation regime, shown for increasing excitation fluence of 10 nJ/cm<sup>2</sup> (light green), 60 nJ/cm<sup>2</sup> (light blue), 150 nJ/cm<sup>2</sup> (yellow), 310 nJ/cm<sup>2</sup> (dark green) and 600 nJ/cm<sup>2</sup> (dark blue). **b**, PL intensity integrated over the spectral emission range of the uncoupled QDs (blue circles) and coupled QDs (red circles) in a log-log plot and the total emitted intensity (yellow circles). Fits to the data reveal a perfectly linear behaviour, as represented by a fitted power-law exponent  $m$  of 1. **c**, Colour-coded PL emission in the high-power excitation regime, shown for increasing excitation fluence of 330  $\mu$ J/cm<sup>2</sup> (light green), 1270  $\mu$ J/cm<sup>2</sup> (light blue), 2130  $\mu$ J/cm<sup>2</sup> (yellow), 3470  $\mu$ J/cm<sup>2</sup> (dark green) and 6330  $\mu$ J/cm<sup>2</sup> (dark blue). **d**, PL intensity integrated over the spectral emission range of the uncoupled QDs (blue) and coupled QDs (red) in a log-log plot and the total emitted intensity (yellow). Fits to the data reveal a power-law behaviour with a linear increase for the SF emission, a slightly sublinear increase for the uncoupled QDs and a less sublinear increase for the total emitted intensity.

**Extended Data Figure 5 | Gaussian first-order coherence decay and photon bunching in pulsed excitation of CsPbBr<sub>3</sub> QD superlattices.** **a**, First-order coherence of the coupled QD emission extracted from the fringe contrast of the interferograms as a function of differential delay time between the arms of a Michelson interferometer, revealing a mixture of Gaussian (Kubo) and exponential decay (for some of the superlattices). **b**, Second-order photon correlation measurement of the coupled QD emission from a single superlattice showing photon bunching at zero delay under pulsed excitation with a 40 MHz repetition rate.

**Extended Data Figure 6 | SF in CsPbBr<sub>2</sub>Cl QD superlattices.** **a**, Band-pass filtered PL spectra of uncoupled QDs (blue) and coupled QD emission (red) of CsPbBr<sub>2</sub>Cl perovskite superlattices. **b**, Second-order photon correlation measurement of uncoupled QDs (top panel,  $g^{(2)}(\tau) = 1$ ) showing flat correlation function, and the coupled QD emission peak band (lower panel,  $g^{(2)}(0) = 1.15$ ) showing photon bunching.

**Extended Data Figure 7 | SF decay and dynamic red-shift of CsPbBr<sub>3</sub> QD superlattices.** **a**, PL spectra (integrated over 2 ps time window) at different time delays in a semi-log scale. **b**, The PL spectra are fitted to a single Gaussian peak function, and the fitted peak amplitude as a function of the emission energy is plotted for various excitation densities. Green arrows indicate the time evolution of the emission peak. The black dashed line denotes the mean energy at the lowest excitation density, and the grey shaded area is the peak's FWHM. **c**, Fitted peak centre energy as a function of time for various excitation densities. **d**, Fast and slow PL decay time

572 components  $\tau_1$  and  $\tau_2$  of the SF bi-exponential fit model as a function of excitation density in a semi-log plot. The  
573 error bars represent the parameters' fit uncertainty.

574 **Extended Data Figure 8 | Burnham–Chiao ringing behaviour in CsPbBr<sub>2</sub>Cl QD superlattices.** **a**, Streak  
575 camera image of SF dynamics obtained with high excitation density of 1600  $\mu\text{J}/\text{cm}^2$ . **b**, Extracted time-resolved  
576 emission intensity traces for three different excitation powers. Solid lines are best-fits to a model that employs a  
577 bi-exponential decay function with damped oscillations. **c**, *Top*: Effective SF decay (blue circles) as a function of  
578 the excitation power density fitted according to the SF model (solid blue line). *Middle*: Red circles represent the  
579 peak SF emission intensity that increases super-linearly with excitation power, corresponding to a power-law  
580 dependence with an exponent  $\alpha = 1.3 \pm 0.1$  (solid dark-red line). *Bottom*: The extracted delay time  $\tau_D$  (green  
581 circles) decreases at high excitation power due to the increased interaction among the emitters. The green solid  
582 line is the best fit according the model described in the Methods section. The error bars represent the  
583 parameters' fit uncertainty.

584


585 **Extended Data Figure 9 | SF decay and dynamic red-shift of CsPbBr<sub>2</sub>Cl QD superlattices.** **a**, PL spectra  
586 (integrated over 2 ps time window) at different time delays in a semi-log scale. **b**, The PL spectra are fitted to a  
587 single Gaussian peak function, and the fitted peak amplitude as a function of the emission energy is plotted for  
588 various excitation densities. Green arrows indicate the time evolution of the emission peak. The black dashed  
589 line denotes the mean energy at the lowest excitation density, and the grey shaded area is the peak's FWHM.  
590 **c**, Fitted peak centre energy as a function of time for various excitation densities. **d**, Fast and slow PL decay time  
591 components  $\tau_1$  and  $\tau_2$  of the SF bi-exponential fit model as a function of excitation density. The error bars  
592 represent the parameters' fit uncertainty.

593

594 **Extended Data Figure 10 | PL decay from a control sample of diluted CsPbBr<sub>3</sub> QD.** **a**, Streak camera  
595 measurement of a control sample prepared by spin-coating a low concentration of CsPbBr<sub>3</sub> QD dispersed in  
596 polystyrene such that no QD coupling is realized. The excitation conditions were comparable to Figure 5, using  
597 an excitation density of 1600  $\mu\text{J}/\text{cm}^2$ . The comparably long decay requires that on the streak camera a longer  
598 time range with lower temporal resolution compared to the measurement in Figure 5 has to be used. The  
599 absence of dynamic red-shift, accelerated decay and ringing proves that the observed SF features cannot be  
600 explained by single QD physics but are a multi-particle effect. **b**, Time-resolved PL trace (blue) obtained from  
601 this streak data. For direct comparison, the equivalent data from a superlattice sample showing SF (Figure 5b,  
602 1200  $\mu\text{J}/\text{cm}^2$ ) is shown (red). Inset: Instrument response function of the streak camera. Using the same  
603 instrument settings as for the superlattices measurement, the temporal response of the streak camera using  
604 scattered light from a 100 fs laser pulse at 400 nm gives a Gaussian-shaped instrument response with a FWHM  
605 of 4.3 ps (Gaussian fit is shown as red solid line).

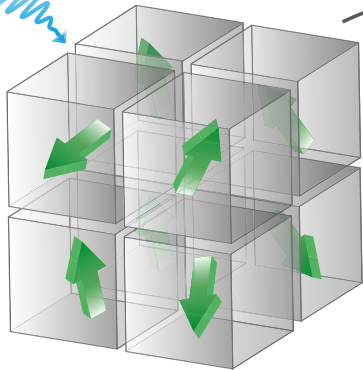
606

Excitation

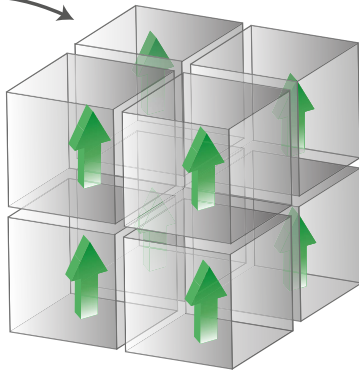


Establish coherence via photon field

$(\tau_D)$

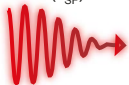


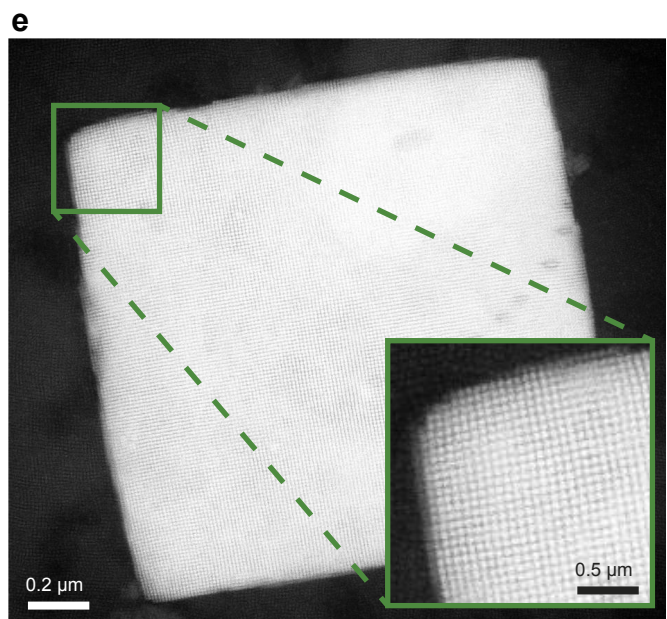
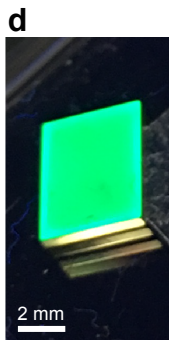
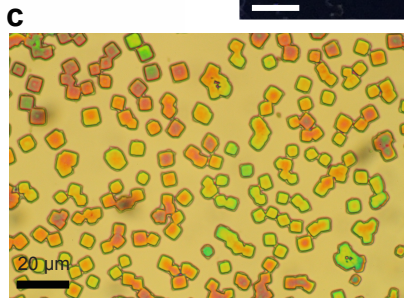
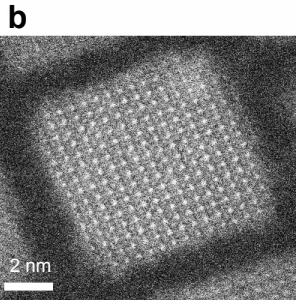
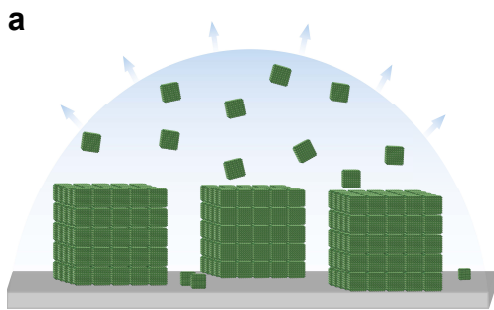
Uncorrelated dipoles

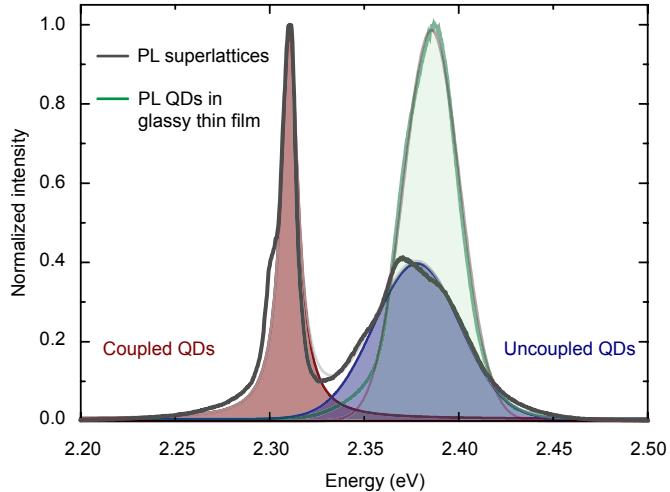
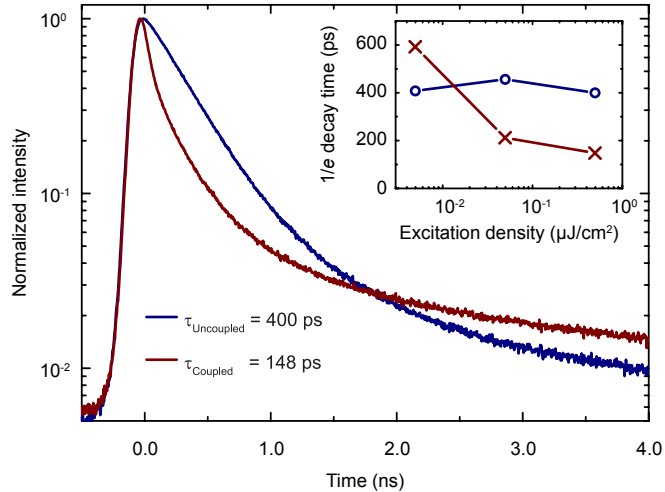


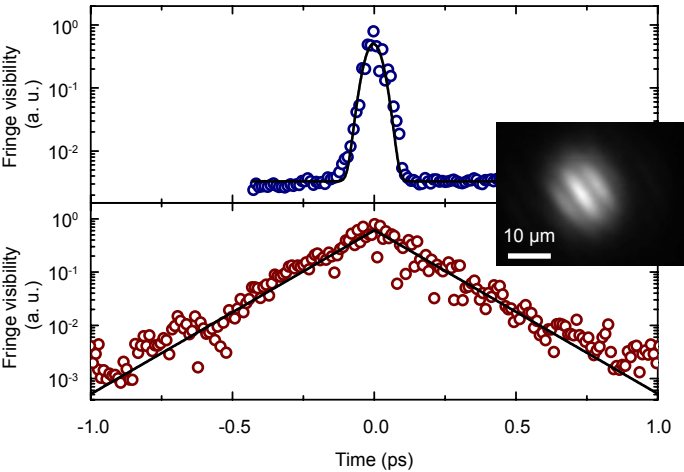
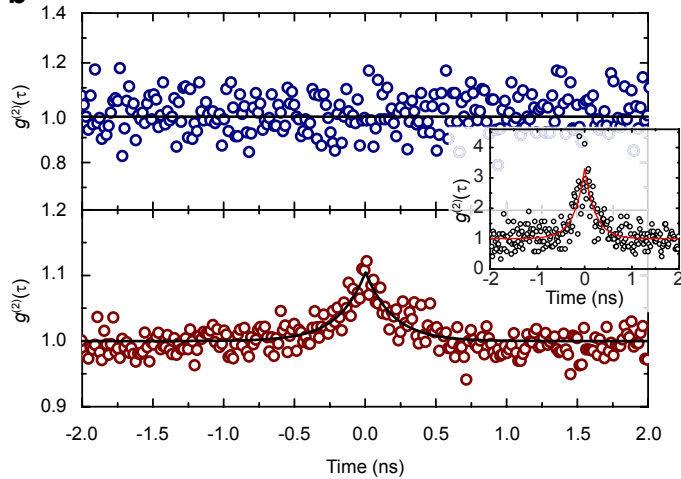
Correlated dipoles

Superfluorescence  
 $(\tau_{SF})$

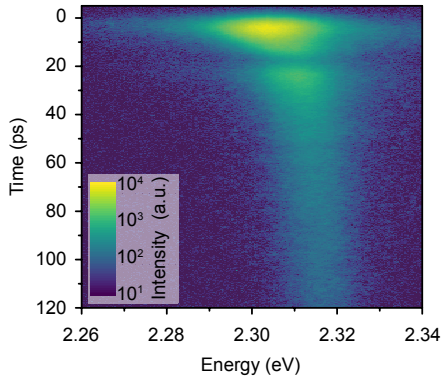
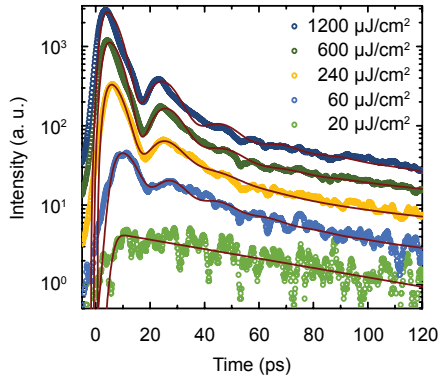




**a****b**

**a****b**



**a****b****c**